Graphical Abstract

Optical properties of annealed nearly percolated Au thin films

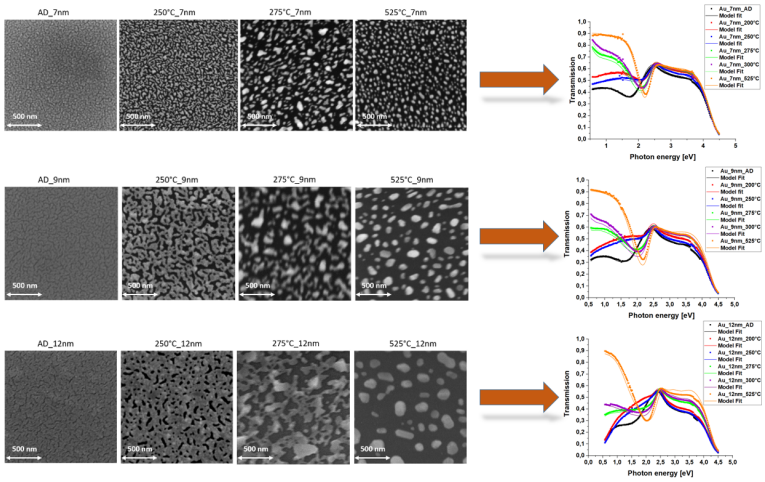

Highlights

Optical properties of annealed nearly percolated Au thin films

- The optical response of annealed Au films around the percolation threshold is studied
- Dewetting mechanisms investigated by combining ellipsometry, AFM and SEM
- Film compactness increases before depercolation temperature is reached
- Metal-dielectric transition enables broad optical response tuning for photonics

Optical properties of annealed nearly percolated Au thin films

Elizabeth Hedl[a,b], Vesna Blažek Bregović[a], Iva Šrut Rakić[c], Šimun Mandić[c], Željko Samec[a], Alexander Bergmann[b], Jordi Sancho-Parramon[a,*]

[a] *Ruđer Bošković Institute, Bijenička cesta 54, Zagreb 10000, Croatia*
[b] *Institute of Electrical Measurements and Sensor Systems, Graz University of Technology, Inffeldgasse 33/I, Graz 8010, Austria*
[c] *Surfaces, Interfaces and 2D Materials Research Group, Institute of Physics, Bijenička 46, Zagreb 10000, Croatia*

Abstract

The optical properties evolution of thermally annealed gold (Au) discontinuous films is investigated and correlated with morphological changes. Nearly percolated Au films with different mass thicknesses are deposited by electron beam evaporation and annealed at temperatures ranging from 200 °C to 525 °C at normal atmosphere. Optical characterization is carried out using transmittance and spectroscopic ellipsometry measurements and film morphology is analyzed with scanning electron microscopy (SEM) and atomic force microscopy (AFM). Film depercolation takes place at temperatures between 250 °C and 300 °C depending on the deposited mass thickness. Annealing at lower temperatures improves film connectivity and quenches the localized plasmon resonance of isolated nanostructures. High-temperature annealing results in well-separated particles with significantly different size distributions depending on the deposited mass thickness, indicating that annealing induces dewetting with different pathways depending on the initial film morphology. The optical properties reflect the interplay among these morphological modifications displaying a large variation for films annealed around the temperature where depercolation takes place. These results evidence that the optical response of nearly-percolated Au films can be broadly tuned in a simple manner, making these samples attractive candidates for

*Corresponding author
Email address: jsancho@irb.hr (Jordi Sancho-Parramon)

Version accepted for publication in Optical Materials

lithography-free photonic applications.

Keywords: Au thin films, percolation, dewetting, spectroscopic ellipsometry, dielectric function

1. Introduction

Discontinuous metal films have gained renewed attention due to their unusually rich optical response that includes localized surface plasmon resonance of isolated clusters, formation of electromagnetic hot-spots at the gap between closely located metal surfaces, and reduced plasma frequency [1, 2]. These films have been proposed as promising candidates for the practical implementation of novel photonics applications because they are suitable for large-scale manufacturing using well-established thin film technology. Thus, discontinuous metal films have been used to devise lithography-free metasurfaces [3, 4], structural colors [5, 6, 7, 8], selective absorbers [9, 10] and different types of sensors [11, 12, 13]. Plasmonic-based enhancement in solar energy conversion [14, 15] is another key application of metal islands films for they can be easily incorporated in the fabrication process of most planar photovoltaic devices [16] and also act as semi-transparent front contacts [17]. In this framework, Au plays a central role as the preferred material of choice due to its high chemical stability compared to other plasmonic materials [18].

Special interests deserve metal films with nearly-percolated morphology. At the percolation threshold, discontinuous films undergo a dielectric to metal transition that translates into a large variety of the optical response in the long-wavelength range [19, 20, 21]. For instance, the real part of the dielectric function can reach very high positive values just below the percolation threshold, which has been used to produce ultra-thin anti-reflective coatings [22]. The percolation transition has been usually investigated by varying the amount of deposited metal [20, 23, 24, 25] or by solid-state dewetting of percolated or compact films [26, 27, 28, 29, 30]. Thermally-induced dewetting of continuous films starts with the appearance of pinholes, their broadening and expansion and, finally, in the formation of isolated particles [31, 32]. The process appears to strongly depend on the initial film morphology [33]. Thus, it has been observed that films just above the percolation threshold experience different dewetting pathways depending on the deposited mass thickness [34]. As a consequence, high-temperature annealing can result in diverse particle size and shape distributions that make the films suitable for

either absorption or scattering-based sensing [35].

In this work we analyze the evolution of optical properties of nearly percolated Au thin films produced by e-beam evaporation and subjected to annealing at different temperatures. In particular, the focus is placed at the temperature range in which films become depercolated, i.e., when the conductive to insulating transition takes place. We show that the use of spectroscopic ellipsometry, a highly sensitive technique for thin film characterization, enables deeper insights than in the case of standard photometric measurements. Thus, parameters such as plasma frequency, free electron damping and film effective thickness are precisely determined. Thus, we confirm and track the different dewetting mechanisms that can occur depending on the deposited mass thickness. Furthermore, an increase in film connectivity is observed before depercolation takes place. High-temperature annealing results in the formation of isolated particle distributions. These observations are confirmed by different morphological and structural characterization techniques, namely SEM and AFM. The obtained insights help understanding the connection between morphology and films structure with the optical response and thus provide guidelines for optimizing the fabrication conditions for specific purposes. Overall, this study illustrates the rich variation of optical properties that can be achieved in films around the percolation threshold by simple thermal treatments, as a prior step towards their practical implementation in photonics applications.

2. Experimental

Glass microscope slides (Menzel) were cut into pieces of 2 cm x 1 cm that were used as substrates for film deposition. The substrates were cleaned with ethanol, wiped with cotton, and puffed with nitrogen. Thin films were fabricated by electron beam evaporation using a modified Leybold chamber. First, a 70 nm SiO_2 film was deposited on the glass substrates to provide the same growth conditions for Au islands regardless of the substrate batch. After that, Au films with mass thickness of 7, 9, or 12 nm were deposited. The amount of deposited material was determined from mass thickness increment by a quartz-crystal thickness monitor. Deposition rates were 10 Å/s for SiO_2 and 1 Å/s for Au and base pressure was $3.5 \cdot 10^{-5}$ mbar. No pre-heating was applied to the substrates.

Thermal annealing of the samples was done for 1 hour at normal atmosphere at temperatures of 200 °C, 250 °C, 275 °C, 300 °C and 525 °C in

a Lindberg/Blue M furnace. This temperature range was selected in order to provide enough thermal energy to induce modifications on the film morphology that could be detected by optical measurements and at the same time avoid glass surface modifications, i.e., the maximum temperature was set below the glass transition temperature ~~the glass transition temperature~~. Samples were left to cool for 1 hour before removing from the furnace.

Normal incidence transmittance and spectroscopic ellipsometry measurements at incidence angles of 45°, 55° and 65° in the spectral range between 0.57 and 5 eV were taken with a V-VASE ellipsometer (J.A. Woollam, Lincoln, NE, USA). Au films were modelled as homogeneous medium as depicted in 1 with effective dielectric function ϵ_{eff} (or, alternatively, effective complex refractive index $N_{eff} = \sqrt{\epsilon_{eff}}$), represented with a multiple oscillator model as presented elsewhere [25]:

$$\epsilon_{eff}(E) = \epsilon_{\infty} - \frac{\omega_p^2}{E(E+i\gamma)} + \sum_{k=1}^{n} \left[\epsilon_{GR,k}(E) + i\epsilon_{GI,k}(E)\right] \tag{1}$$

with

$$\epsilon_{GI,k}(E) = A_k \left[\exp^{-\left(\frac{E-E_k}{B_k}\right)^2} - \exp^{-\left(\frac{E+E_k}{B_k}\right)^2}\right] \tag{2}$$

$$\epsilon_{GR,k}(E) = \frac{2}{\pi} P \int_0^{\infty} \frac{\xi \epsilon_{GI,k}(\xi)}{\xi^2 - E^2} d\xi \tag{3}$$

where E is the photon energy. The first term on the right-hand side of Eq. 3, ϵ_{∞}, accounts for the polarization mechanisms that occur at photon energies above the measured spectral range. The second term is the Drude model that describes the metal-like response of percolated films defined through the plasma frequency (ω_p) and the damping term (γ). Finally, the last term is a sum of Gaussian oscillators that is used to model localized surface plasmon resonance and interband transitions. Each Gaussian oscillator is defined through its amplitude (A_k), central energy (E_k) and broadening (B_k). . ~~In essence, the model includes different 3-parameter Gaussian oscillators to represent localized surface plasmon resonances and interband transitions while the infrared response of percolated films was accounted by a Drude term defined by two parameters: the plasma frequency (ω_p) and the damping term (Γ).~~. In order to obtain effective thicknesses and parameters describing the effective optical constants, transmittance and ellipsometric measurements were analyzed with the WVASE32 software (J.A. Woollam, Lincoln, NE, USA).

The combination of transmittance and ellipsometric measurements has been previously shown to provide reliable results in the characterization of very thin absorbing films [36].

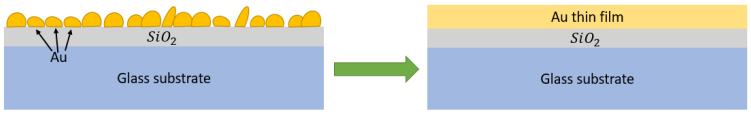

Figure 1: Optical model used for fitting of ellipsometric data. The discontinuous island films is represented by an homogeneous film with effective optical constants and effective thickness.

Morphological changes of the samples were tracked by SEM and AFM. Tescan Vega3 LMU (Brno, Cech Republic) with tungsten filament at working distances between 2 and 5 mm, 5-30 kV acceleration voltages was used for SEM measurements. AFM images were acquired using NeaSpec (Munich, Germany) IR-neaSCOPE+fs AFM in AC mode. Each sample was imaged with both SEM and AFM on at least three different location with a maximum field of view of around 6 μm to check sample homogeneity and get adequate statistics. On each region higher magnification images were also taken to get better resolution of smaller details. We present here SEM images with the field of view of 1.6 μm, and AFM images with 1 μm field of view as on that magnification the drastic change in the sample topography is visualized the best. AFM probes were obtained from Nano World (ARROW-NCR with a radius of curvature of less than 10 nm, nominal spring constant of 42 N/m, and a nominal resonant frequency of 285 kHz). Conductive AFM (cAFM) measurements were acquired using JPK (Berlin, Germany) NanoWizard 4 Ultra AFM in contact mode with 15.2 nN setpoint. The Au layer was contacted directly from the top side using metal clamp integrated in the sample holder through which the bias voltage was applied. Conductive Pt/Ir coated AFM probes were obtained from Nano World (ARROW-EFM with curvature less than 25 nm, nominal spring constant of 2.8 N/m, and a nominal resonant frequency of 75 kHz). Images were subsequently processed using the Gwyddion software [37]. To extract grain size distributions we first used watershed feature to determine the grain positions and then use *Grain distribution* feature to extract histograms of the following: root mean square values of grain heights, grain surface area and calculated radius assuming

spherical shape [38, 39].

3. Results and discussion

Figure 1 shows the transmittance spectra of the as-deposited and annealed samples. The transmittance decrease above 3.5 eV is related to the glass band gap. All samples show a wide shoulder around 3 eV connected with Au interband transitions [40]. As deposited samples show a minimum between 1.5 and 2 eV that broadens and red-shifts with the increasing deposited mass thickness, suggesting resonances of isolated nanostructures in the film. In the 12 nm sample, this dip appears as a shoulder. The low energy region is characterized by a decrease of transmittance as the photon energy is reduced. This behavior is typical of connected metal films and hence it could be interpreted as a signature of percolation [19].

Annealing at moderate temperatures quenches the transmittance dip. However, the dip reappears at larger photon energies when annealing is conducted at higher temperature. Additionally, transmittance at low photon energies monotonically increases with annealing temperature, except for the samples annealed at 250 °C. This increase of transparency in the infrared range could be interpreted on the basis of a reduction of film connectivity [41]. The described features are qualitatively common to all samples and therefore evolution of the transmittance spectra suggests similar morphological changes regardless of the mass thickness.

Fitting of ellipsometric data allows determining the real (ε_1) and imaginary (ε_2) parts of the film effective dielectric function (Figure 2). It will be shown that several important features are not fully consistent with the suggested interpretation of transmittance spectra discussed above. The metal-to-dielectric transition is characterized by a change on the sign of the real part of the dielectric function at low energies, from negative to very high positive values [20]. In addition, in a percolated metal network the real part of the dielectric function progressively becomes more negative when the photon energy is reduced. Thus, the 7 nm as-deposited sample appears to be very closely located to the percolation threshold because its infrared response can not be clearly ascribed either to the metallic or dielectric regime. On the other hand, some of the moderately annealed samples show more negative values than the as-deposited ones, indicating an increase of sample connectivity. This is most clearly seen by the evolution of the parameters of the Drude model (Table 1), that was included in the model of the effective di-

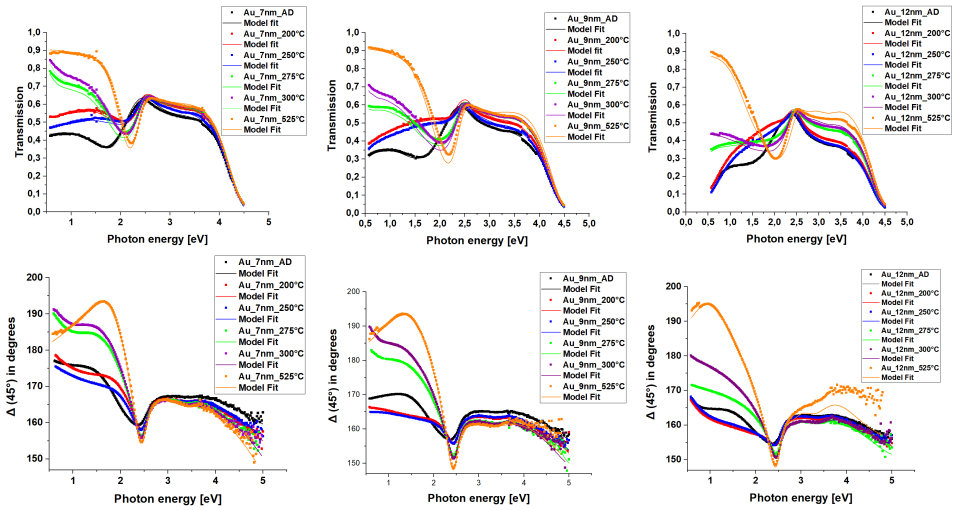

Figure 2: Transmittance (top) and ellipsometic angle Δ (bottom) spectra for as-deposited (AD) and annealed samples for 7 (left), 9 (middle) and 12 (right) nm mass thickness at the indicated temperatures. Symbols and solid lines represent experimental data and best fits respectively. ~~Transmittance spectra at normal incidence for the as-deposited (AD) and annealed samples for 7 (a), 9 (b) and 12 (c) nm mass thickness at the indicated temperatures.~~

electric function only if it was able to improve the fit quality. In case of the 7 nm mass thickness samples, only the one annealed at 250 °C shows a clear Drude signature while for the as-deposited sample and the sample annealed at 200 °C the infrared response turns out to be better described by a Gaussian oscillator located at low energies (below 0.5 eV). In the case of samples with 9 and 12 nm mass thickness the most percolated sample is the one annealed at 250 °C, showing the largest plasma frequency as well as the most reduced damping in the Drude term. Therefore, the film connectivity turns out to improve for moderate temperature annealing before dewetting takes place, what can be connected with partial islands coalescence [29] and closing of voids in weakly percolated films [41]. In the case of the sample with 12 nm mass thickness, the increase of sample connectivity upon moderate annealing is further supported by a decrease of effective thickness (Table 1). It should be noted that, in general, an increase of the effective film thickness and lower metallic contribution in the effective optical constants should be expected upon annealing if islands become larger and less connected. Thus, the decrease of effective thickness in this sample points out to that the film

becomes more compact at the lower annealing temperatures. It should be noted that the progressive increase of film connectivity before depercolation occurs can not be detected by the analysis of transmittance data only. Thus, the increase of transmittance at low energy regions for moderate annealing should be associated to a reduction of losses (lower imaginary part of the effective dielectric function) due to the increase of film compactness.

Above 275 °C the real part of the dielectric function is positive in the infrared range and the strength of the resonance in the visible increases with annealing temperature, indicating that the films are in the insulating phase and progressively transform into a morphology of well-separated nano-structures. The decrease of film compactness is further supported by the large increase of the film effective thickness and less intense interband transitions in the high energy range, what can not be deduced by the information provided by transmittance measurements. The peak in the imaginary part for the 12 nm sample annealed at 525 °C is much broader than in case of samples with smaller thickness annealed at the same temperature. This observation points out the presence of significantly larger particles and/or particles with a very large aspect ratio. Such observation if further supported by the worse fitting quality of ellipsometric data as quantified by the mean-squared error (Table 1) that can be explained by significant scattering losses that can not be accounted by the homogeneous film model.

In order to confirm the observations suggested by the analysis of the ellipsometric modelling presented above, SEM micrographs are shown in Figure 3. None of the as-deposited films appears to be fully compact and the degree of percolation/film connectivity appears to increase with the mass thickness as it corresponds to the Volmer-Weber growth mechanism [42]. A similar trend is observed for samples annealed at 250 °, yet displaying a qualitatively different morphological arrangement. Annealing at this temperature causes the voids between metal regions to expand and partially become connected, leaving place to a more clearly connected network in comparison to the as-deposited films. This observation is in good correspondence with the plasma frequency increase deduced from ellipsometry. Additionally, the increase of film connectivity is accompanied by a reduced presence of isolated structures, explaining the quenching of localized resonances detected in the analysis of optical measurements.

In case of samples annealed at 250 °C, the morphology of the 12 nm mass thickness sample is qualitatively different than the one observed for samples with mass thickness of 7 and 9 nm. In case of smaller mass thickness voids

7 nm Au film					
T [°C]	d_{eff} **[nm]**	ω_p^2**[eV^2]**	γ**[eV]**	$\mathbf{R}_{rms}$ **[nm]**	**MSE**
RT	9.9 ± 0.1	–	–	0.84	2.13
200	11.6 ± 0.2	–	–	–	3.55
250	12 ± 0.2	17 ± 6	1.1 ± 0.4	–	2.90
275	13.5 ± 0.2	–	–	6.21	2.81
300	14.9 ± 0.3	–	–	2.84	2.81
525	20.3 ± 0.5	–	–	10.31	3.00
9 nm Au film					
T [°C]	d_{eff} **[nm]**	ω_p^2**[eV^2]**	γ**[eV]**	$\mathbf{R}_{rms}$ **[nm]**	**MSE**
RT	11.4 ± 0.1	23 ± 8	0.17 ± 0.08	1.43	1.73
200	11.9 ± 0.1	18.9 ± 0.2	0.167 ± 0.006	–	2.65
250	12.3 ± 0.1	22.7 ± 0.2	0.117 ± 0.004	–	2.56
275	16.9 ± 0.2	–	–	9.53	3.32
300	18.2 ± 0.2	–	–	–	3.95
525	30.8 ± 0.8	–	–	13.77	4.17
12 nm Au film					
T [°C]	d_{eff} **[nm]**	ω_p^2**[eV^2]**	γ**[eV]**	$\mathbf{R}_{rms}$ **[nm]**	**MSE**
RT	14.3 ± 0.12	47.0 ± 0.5	0.088 ± 0.006	1.45	1.90
200	13.6 ± 0.1	46.8 ± 0.3	0.052 ± 0.003	–	1.88
250	13.9 ± 0.1	51.2 ± 0.3	0.049 ± 0.002	–	1.47
275	17.1 ± 0.14	13.9 ± 0.2	0.44 ± 0.01	11.6	2.14
300	18.8 ± 0.26	–	–	–	2.44
525	32.4 ± 1.4	–	–	24.5	7.24

Table 1: Summary of results extracted from ellipsometric (effective thickness, d_{eff}, plasma frequency ω_p, Drude damping term γ) and AFM (film roughness, R_{rms}) analysis of the investigated samples. The ellipsometric data fitting quality (mean-squared error, MSE) is displayed in the last column.

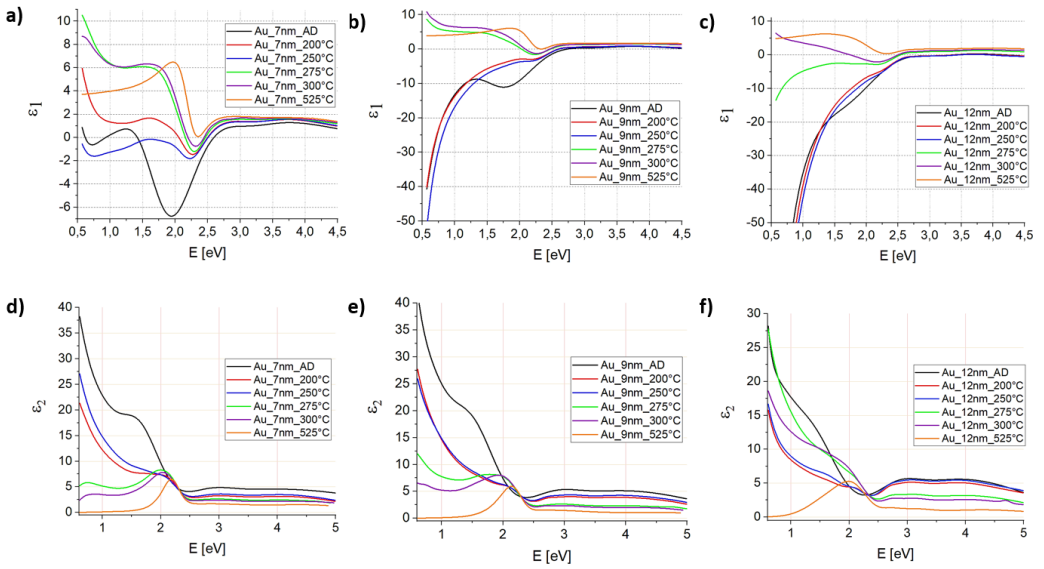

Figure 3: Real (ε_1, top) and imaginary (ε_2, bottom) part of effective dielectric function of 7 (left), 9 (middle) and 12 (right) nm gold thin film before and after annealing at different temperatures.

widen and form a broad distribution of irregular particles. On the other hand, a distribution of holes within the percolated film is formed in case of large mass thickness, in line with observations reported in [41]. This different morphology can be connected to the reduced damping term (Table 1) that in the case of 12 nm samples reaches values close to bulk Au, regardless the plasma frequency film, i.e., film compactness, is clearly below bulk values [40]: although the film is not compact, its hollowness does not contribute to additional damping when free electrons are drifted by an external electric field. This different dewetting mechanism has a strong effect on the film morphology of samples annealed at large temperatures: smaller islands are observed in the case of small initial mass thickness while large particles are obtained for the sample with 12 nm mass thickness in agreement with the results of optical characterization and supporting previous observations [34].

Complementary morphological characterization was obtained by AFM (Figure 4). The structure of as-deposited films is not well resolved, probably due to tip-convolution effects that do not allow to map the voids between metal regions. However, in the case of annealing at large temperatures, i.e. with islands-like morphology, AFM provides relevant information on

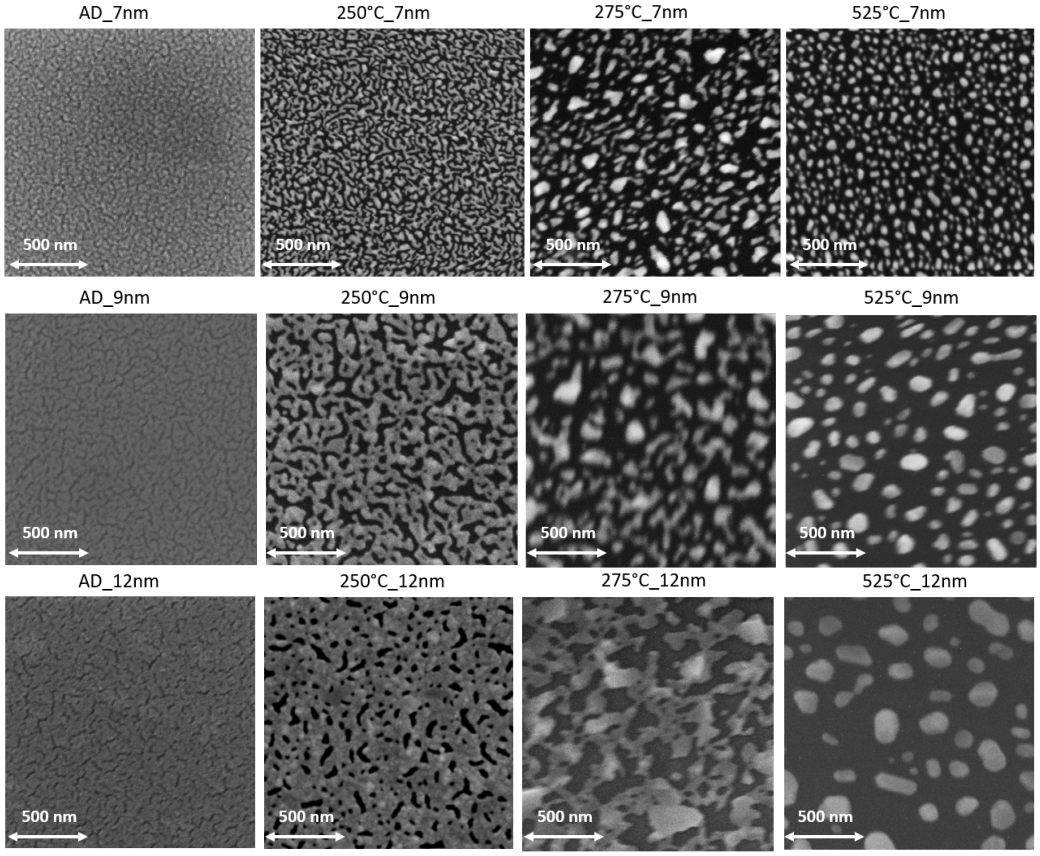

Figure 4: SEM image of sample surfaces for samples with different mass thickness (rows) and annealed at different temperatures (columns) for 1 hour (500 nm scale, SEM HV: 10.0 kV with magnitude around 80 kx).

particle height and shape. Thus, film roughness (last column in Table 1) increases when dewetting takes place and is particularly high in the case of samples with 12 nm thickness annealed at 525 °C, as a consequence of the large particles observed in this case. Furthermore, AFM shows that these islands have flat tops, indicating that the dewetting mechanism for this kind of films is accompanied by crystallization, in the line of previous observations [34]. The AFM size distribution (effective radius in the plane parallel to the substrate surface) is shown in Figure 5. The films with 7 and 9 nm mass thickness display small and medium-sized particles that are result of islands formation from the highly irregular structures observed at moderate annealing temperatures [33]. On the other hand, the 12 nm film has a broader size distribution with significantly larger particles, explaining the wider and red-shifted localized surface plasmon resonance observed in the optical spectra. The presented analysis on Figure 5 can indicate bimodal distribution that might result from a process involving different thermal-induced dewetting mechanisms.

Finally, film connectivity was analyzed by conductive AFM measurements for the sample with 12 nm mass thickness (Figure 6). In the case of the sample annealed at 275 °C is possible to see that topography does not have a full correspondence with the islands electrical conductivity map. In fact, it is observed that a fraction of islands are electrically isolated from the metal network. This observation can not be assessed from SEM micrographs or standard AFM topographic measurements, but it explains the reduced plasma frequency and increased damping term revealed by ellipsometry for this sample (Table 1). On the other side, the sample annealed at 250 °C shows a larger density of conductive islands, i.e. lower density of non-connected regions, in agreement with the higher plasma frequency as determined by ellipsometry.

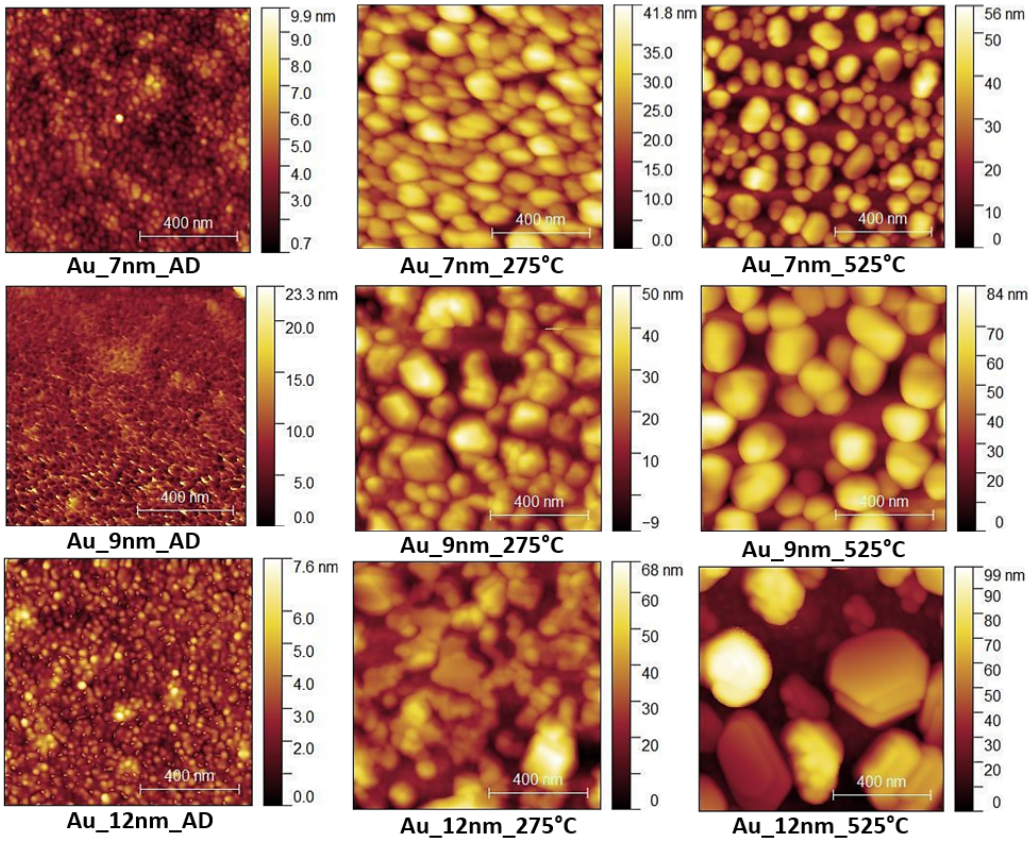

Figure 5: AFM images of the 7 nm, 9 nm and 12 nm gold films (rows) as-deposited and annealed at different temperatures (columns). All images are presented at the same scale.

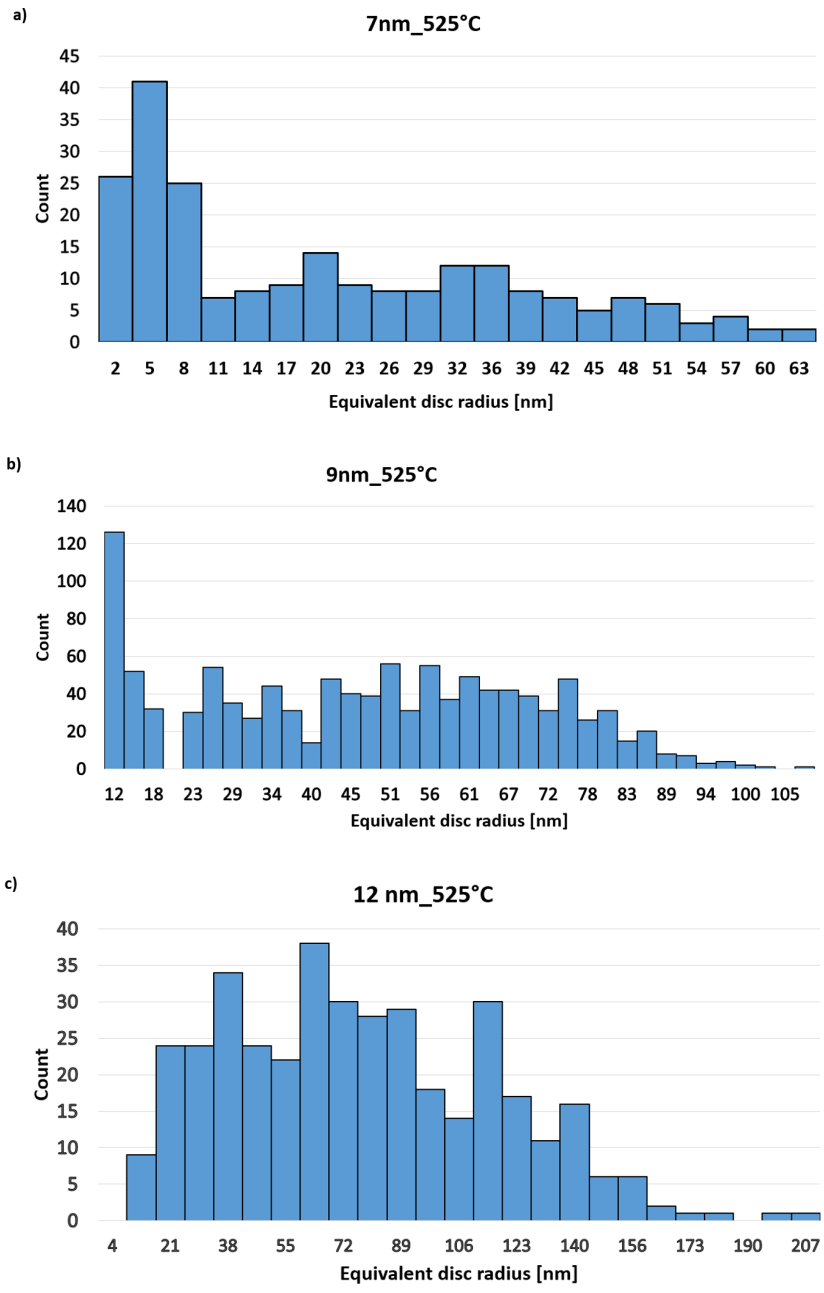

Figure 6: Particle effective radius distributions from AFM data for the samples annealed at 525 °C with 7 (top), 9 (middle) and 12 (bottom) nm mass thickness.

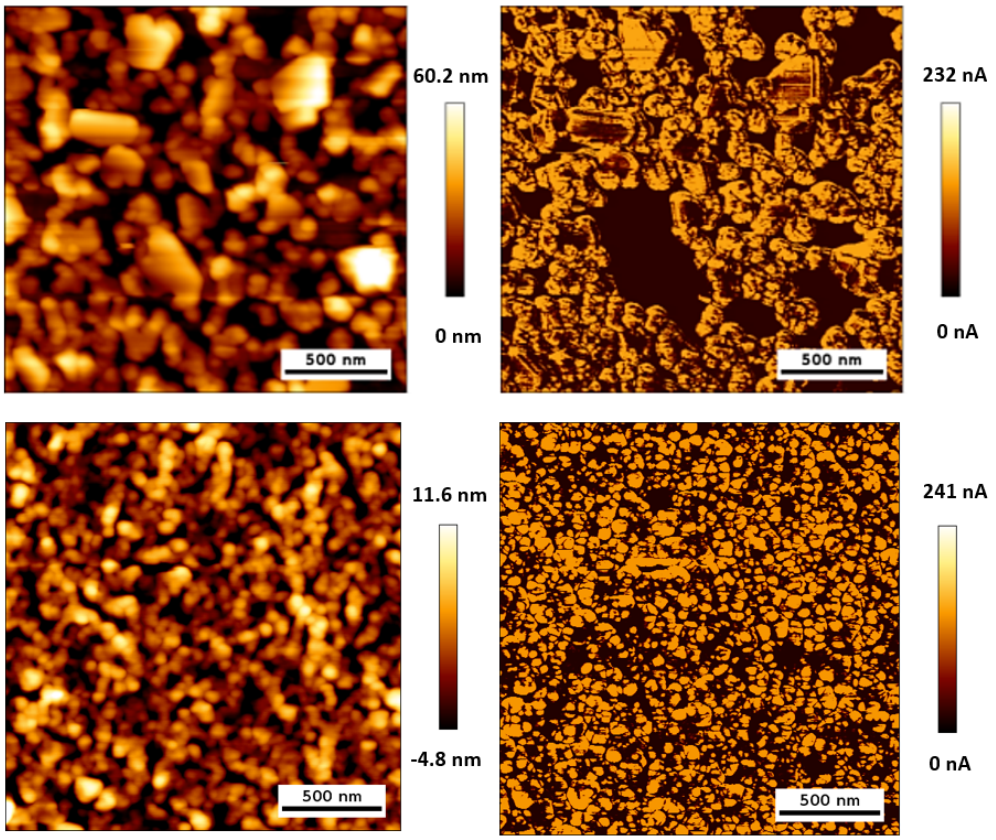

Figure 7: AFM topography (left) and conductivity (right) measurements for the sample with 12 nm mass thickness annealed at 275 °C (top) and 250 °C (bottom) using a potential of -0.5V.

4. Conclusions

Optical response of annealed nearly percolated gold films widely varies with the annealing temperature and it has been showed that at moderate temperatures the film compactness improves resulting in increased percolation and a more clear Drude-like response of the films, together with quenched plasmon resonances of isolated particles. Depercolation takes place at intermediate annealing temperatures (250 °C to 300 °C). Higher annealing temperatures produce films of well-separated particles characterized by a single localized surface plasmon resonance. Depending on the deposited mass thickness, the dewetting mechanism leads to qualitative different morphology for

films annealed at moderate and high temperatures. The present results confirm the suitability of spectroscopic ellipsometry as a non-destructive technique able to provide detailed insights on the evolution of film morphology, as corroborated by the results of SEM and AFM investigations. The wide variation of the optical properties in films around the percolation threshold is especially important in the infrared range. In summary, this paper showed that thermal treatment of nearly-percolated films are an interesting approach to tailor optical properties in view of potential photonic applications and that tuning of optical response in the conductive-to-insulator transition can be explored by simple annealing in a relatively wide temperature range.~~It has been shown that the optical response of annealed nearly percolated gold films widely varies with the annealing temperature. At moderate temperatures the film compactness improves resulting in increased percolation and a more clear Drude-like response of the films together with quenched plasmon resonances of isolated particles. Depercolation takes place at intermediate annealing temperatures (250 °C to 300 °C). Higher annealing temperatures produce films of well-separated particles characterized by a single localized surface plasmon resonance. Depending on the deposited mass thickness, the dewetting mechanism leads to qualitative different morphology for films annealed at moderate and high temperatures. The present results confirm the suitability of spectroscopic ellipsometry as a non-destructive technique able to provide detailed insights on the evolution of film morphology, as corroborated by the results of SEM and AFM investigations. The wide variation of the optical properties in films around the percolation threshold is especially important in the infrared range. Tuning of optical response in the conductive-to-insulator transition can be explored by simple annealing in a relatively wide temperature range, making thermal treatment of nearly-percolated films an interesting approach to tailor optical properties in view of potential photonic applications.~~

5. Funding

The authors thank the financial support of the Croatian Science Foundation through the grant number IP-2019-04-5424. I.Š.R. and Š.M. acknowledge financial support by the Center of Excellence for Advanced Materials and Sensing Devices (ERDF Grant No. KK.01.1.1.01.0001) and the Center for Advanced Laser Techniques (EFRR Grant No.KK.01.1.1.05.0001).

References

[1] V. M. Shalaev, Optical properties of nanostructured random media, Vol. 82, Springer Science & Business Media, 2002.

[2] R. Singer, A. Leitner, F. Aussenegg, Structure analysis and models for optical constants of discontinuous metallic silver films, JOSA B 12 (2) (1995) 220–228.

[3] A. Ghobadi, T. G. U. Ghobadi, E. Ozbay, Lithography-free metamaterial absorbers: opinion, Optical Materials Express 12 (2) (2022) 524–532.

[4] G. A. López-Muñoz, A. Cortés-Reséndiz, J. Ramón-Azcón, A. Rydosz, Scalable, lithography-free plasmonic metasurfaces by nanopatterned/sculpted thin films for biosensing, Frontiers in Sensors (2022) 18.

[5] V. Janicki, T. V. Amotchkina, J. Sancho-Parramon, H. Zorc, M. K. Trubetskov, A. V. Tikhonravov, Design and production of bicolour reflecting coatings with au metal island films, Optics Express 19 (25) (2011) 25521–25527.

[6] D. Franklin, Z. He, P. Mastranzo Ortega, A. Safaei, P. Cencillo-Abad, S.-T. Wu, D. Chanda, Self-assembled plasmonics for angle-independent structural color displays with actively addressed black states, Proceedings of the National Academy of Sciences 117 (24) (2020) 13350–13358.

[7] Y. H. Kim, M. Rahman, J. S. Hwang, H. Ko, J.-Y. Huh, J. Y. Byun, Reflection color tuning of a metal–insulator–metal cavity structure using arc plasma deposition of gold nanoparticles, Applied Surface Science 562 (2021) 150140.

[8] R. Yu, P. Mazumder, N. F. Borrelli, A. Carrilero, D. S. Ghosh, R. A. Maniyara, D. Baker, F. J. García de Abajo, V. Pruneri, Structural coloring of glass using dewetted nanoparticles and ultrathin films of metals, ACS Photonics 3 (7) (2016) 1194–1201.

[9] Z. Li, S. Butun, K. Aydin, Large-area, lithography-free super absorbers and color filters at visible frequencies using ultrathin metallic films, Acs Photonics 2 (2) (2015) 183–188.

[10] J. Nath, E. Smith, D. Maukonen, R. E. Peale, Optical salisbury screen with design-tunable resonant absorption bands, Journal of Applied Physics 115 (19) (2014) 193103.

[11] T. Karakouz, A. B. Tesler, T. A. Bendikov, A. Vaskevich, I. Rubinstein, Highly stable localized plasmon transducers obtained by thermal embedding of gold island films on glass, Advanced Materials 20 (20) (2008) 3893–3899.

[12] H. Sun, M. Yu, X. Sun, G. Wang, J. Lian, Effective temperature sensing by irreversible morphology evolution of ultrathin gold island films, The Journal of Physical Chemistry C 117 (7) (2013) 3366–3373.

[13] V. P. Drachev, M. D. Thoreson, V. Nashine, E. N. Khaliullin, D. Ben-Amotz, V. J. Davisson, V. M. Shalaev, Adaptive silver films for surface-enhanced raman spectroscopy of biomolecules, Journal of Raman Spectroscopy: An International Journal for Original Work in all Aspects of Raman Spectroscopy, Including Higher Order Processes, and also Brillouin and Rayleigh Scattering 36 (6-7) (2005) 648–656.

[14] K. Catchpole, , A. Polman, Plasmonic solar cells, Optics express 16 (26) (2008) 21793–21800.

[15] S. Pillai, , M. Green, Plasmonics for photovoltaic applications, Solar Energy Materials and Solar Cells 94 (9) (2010) 1481–1486.

[16] O. Stenzel, A. Stendal, K. Voigtsberger, C. Von Borczyskowski, Enhancement of the photovoltaic conversion efficiency of copper phthalocyanine thin film devices by incorporation of metal clusters, Solar energy materials and solar cells 37 (3-4) (1995) 337–348.

[17] K. Chopra, P. Paulson, V. Dutta, Thin-film solar cells: an overview, Progress in Photovoltaics: Research and applications 12 (2-3) (2004) 69–92.

[18] P. R. West, S. Ishii, G. V. Naik, N. K. Emani, V. M. Shalaev, A. Boltasseva, Searching for better plasmonic materials, Laser & photonics reviews 4 (6) (2010) 795–808.

[19] Y. Yagil, G. Deutscher, Transmittance of thin metal films near the percolation threshold, Thin Solid Films 152 (3) (1987) 465–471.

[20] M. Hövel, B. Gompf, M. Dressel, Dielectric properties of ultrathin metal films around the percolation threshold, Phys. Rev. B 81 (2010) 035402. doi:10.1103/PhysRevB.81.035402.
URL https://link.aps.org/doi/10.1103/PhysRevB.81.035402

[21] H. Bakkali, E. Blanco, S. Lofland, M. Domínguez, Divergence of the dielectric constant in ultrathin granular metal films near the percolation threshold, New Journal of Physics 22 (8) (2020) 083018.

[22] B. Gompf, J. Beister, T. Brandt, J. Pflaum, M. Dressel, Nanometer-thick au-films as antireflection coating for infrared light, Optics letters 32 (11) (2007) 1578–1580.

[23] J. Sancho-Parramon, V. Janicki, H. Zorc, On the dielectric function tuning of random metal-dielectric nanocomposites for metamaterial applications, Opt. Express 18 (26) (2010) 26915–26928. doi:10.1364/OE.18.026915.
URL http://opg.optica.org/oe/abstract.cfm?URI=oe-18-26-26915

[24] A. J. de Vries, E. S. Kooij, H. Wormeester, A. A. Mewe, B. Poelsema, Ellipsometric study of percolation in electroless deposited silver films, Journal of applied physics 101 (5) (2007) 053703.

[25] J. Sancho-Parramon, B. Okorn, K. Salamon, V. Janicki, Plasmonic resonances in copper island films, Applied Surface Science 463 (2019) 847–853.

[26] J. A. Badán, E. Navarrete-Astorga, R. Henríquez, F. M. Jiménez, D. Ariosa, J. R. Ramos-Barrado, E. A. Dalchiele, Silver nanoparticle arrays onto glass substrates obtained by solid-state thermal dewetting: A morphological, structural and surface chemical study, Nanomaterials 12 (4) (2022) 617.

[27] J. Liu, L. Chu, Z. Yao, S. Mao, Z. Zhu, J. Lee, J. Wang, L. A. Belfiore, J. Tang, Fabrication of au network by low-degree solid state dewetting: Continuous plasmon resonance over visible to infrared region, Acta Materialia 188 (2020) 599–608.

[28] H. Oh, J. Lee, M. Seo, I. U. Baek, J. Y. Byun, M. Lee, Laser-induced dewetting of metal thin films for template-free plasmonic color printing, ACS applied materials & interfaces 10 (44) (2018) 38368–38375.

[29] P. Gadkari, A. Warren, R. Todi, R. Petrova, K. Coffey, Comparison of the agglomeration behavior of thin metallic films on si o 2, Journal of Vacuum Science & Technology A: Vacuum, Surfaces, and Films 23 (4) (2005) 1152–1161.

[30] C. T. Campbell, Ultrathin metal films and particles on oxide surfaces: structural, electronic and chemisorptive properties, Surface science reports 27 (1-3) (1997) 1–111.

[31] H. Sato, S. Shinozaki, Morphology of nuclei and epitaxial behavior of au and ag on mgo, Journal of Vacuum Science and Technology 8 (1) (1971) 159–163.

[32] C. R. Henry, Morphology of supported nanoparticles, Progress in surface science 80 (3-4) (2005) 92–116.

[33] C. V. Thompson, Solid-state dewetting of thin films, Annual Review of Materials Research 42 (2012) 399–434.

[34] A. B. Tesler, L. Chuntonov, T. Karakouz, T. A. Bendikov, G. Haran, A. Vaskevich, I. Rubinstein, Tunable localized plasmon transducers prepared by thermal dewetting of percolated evaporated gold films, The Journal of Physical Chemistry C 115 (50) (2011) 24642–24652.

[35] T. Karakouz, D. Holder, M. Goomanovsky, A. Vaskevich, I. Rubinstein, Morphology and refractive index sensitivity of gold island films, Chemistry of Materials 21 (24) (2009) 5875–5885.

[36] J. N. Hilfiker, N. Singh, T. Tiwald, D. Convey, S. M. Smith, J. H. Baker, H. G. Tompkins, Survey of methods to characterize thin absorbing films with spectroscopic ellipsometry, Thin Solid Films 516 (22) (2008) 7979–7989.

[37] D. Nečas, P. Klapetek, Gwyddion: an open-source software for spm data analysis, Open Physics 10 (1) (2012) 181–188 [cited 2022-06-12]. doi:doi:10.2478/s11534-011-0096-2.
URL https://doi.org/10.2478/s11534-011-0096-2

[38] L. Vincent, P. Soille, Watersheds in digital spaces: an efficient algorithm based on immersion simulations, IEEE Transactions on Pattern Analysis & Machine Intelligence 13 (06) (1991) 583–598.

[39] P. Klapetek, I. Ohlídal, D. Franta, A. Montaigne-Ramil, A. Bonnani, D. Stifter, H. Sitter, Atomic force microscopy characterization of znte epitaxial films, Acta Physica Slovaca 53 (3) (2003) 223–230.

[40] P. B. Johnson, R.-W. Christy, Optical constants of the noble metals, Physical review B 6 (12) (1972) 4370.

[41] A. B. Tesler, B. M. Maoz, Y. Feldman, A. Vaskevich, I. Rubinstein, Solid-state thermal dewetting of just-percolated gold films evaporated on glass: development of the morphology and optical properties, The Journal of Physical Chemistry C 117 (21) (2013) 11337–11346.

[42] N. Kaiser, Review of the fundamentals of thin-film growth, Applied optics 41 (16) (2002) 3053–3060.